EurJIC
European Journal of Inorganic Chemistry

Full Papers
doi.org/10.1002/ejic.202100328

Chemistry Europe
European Chemical Societies Publishing

Predicting the Structural Transition in Medium-Sized Boron Nanoclusters: From Bilayer B_{64}, B_{66}, B_{68}, B_{70}, and B_{72} to Core-Shell B_{74}

Ling Pei[+],[a, b] Qiao-Qiao Yan[+],[a] and Si-Dian Li*[a]

Recent experimental observation of the first bilayer clusters $B_{48}^{-/0}$ reveals a new structural domain in boron nanostructures. Inspired by the previously reported bilayer B_{48}, B_{54}, B_{60}, and B_{62} and based on extensive global-minimum searches and density-functional theory calculations, we predict herein a new series of medium-sized bilayer boron nanoclusters C_2 B_{64} (**I**), D_2 B_{66} (**II**), D_2 B_{68} (**III**), C_1 B_{70} (**IV**), and C_i B_{72} (**V**) which all contain an elongated B_{46} bilayer hexagonal prism at the center with four effective interlayer 2c–2e B–B σ bonds formed between the top and bottom layers and the bilayer to core-shell structural transition at B_{74} where core-shell species start to dominate in thermodynamics, defining the up-limit of the bilayer boron nanoclusters at B_{72}. The newly obtained bilayer C_2 B_{64} (**I**), D_2 B_{68} (**III**), and C_1 B_{70} (**IV**) appear to be systematically more stable than the previously reported cage-like D_{4d} B_{64}, core-shell C_1 B_{68}, and quasi-planar C_{3v} B_{70}, respectively. Detailed bonding analyses indicate that these bilayer species follow the universal bonding pattern of σ+π double delocalization, rendering three-dimensional aromaticity to the systems. The IR, Raman, and UV-vis spectra of the concerned bilayer species are computationally simulated to facilitate their future characterizations.

Introduction

As a prototypical electron-deficient element, boron has a rich chemistry[1] next only to carbon in the periodical table. Persistent joint photoelectron spectroscopy (PES) and first-principles theory investigations in the past two decades have unveiled a rich landscape for size-selected $B_n^{-/0}$ boron clusters from planar or quasi-planar (2D) boron sheets (n=3–38, 41–42),[2] cage-like borospherenes D_{2d} $B_{40}^{-/0}$ and C_3/C_2 B_{39}^-,[3] to bilayer D_{2h} $B_{48}^{-/0}$.[4] The borospherene family has been extended at first-principles theory level to include the B_n^q series (n=36–42, q=n-40) which are all composed of twelve interwoven boron double chains with six hexagons or heptagons on the cage surface in a universal bonding pattern of σ+π double delocalization.[3,5] Seashell-like borospherenes C_2 B_{28}^- and C_s B_{29}^- were late observed in PES measurements as minor isomers competing with their 2D global minimum (GM) counterparts.[6] Following the same structural motif, seashell-like C_s B_{29}^+, C_2 B_{31}^+, C_2 B_{32}, C_2 B_{34}, C_2 B_{35}^+, and C_2 B_{38}^+ were predicted in theory recently.[7] Boron cluster monocations B_n^+ (n=16–25) were shown to possess double-ring tubular geometries in a joint ion-mobility measurements and density functional theory (DFT) investigation.[8] Neutral core-shell B_n clusters C_1 B_{68}, C_1 B_{74}, C_1 B_{80}, D_{3d} B_{98}, C_{2h} B_{100}, C_s B_{101}, D_{3d} B_{102}, C_s B_{111}, C_s B_{112}, C_s B_{113}, and C_s B_{114} with a partially or completely encapsulated icosahedral B_{12} core were predicted to dominate in thermodynamics in a large cluster size range starting from n=68, with C_s B_{112} being the most stable core-shell species in thermodynamics reported to date between B_{68}–B_{130},[9] indicating that an icosahedral B_{12} cage serves as the energetically most favorable "seeds" to form three-dimensional (3D) boron allotropes in bottom-up approaches. B_{84} as an exception was previously predicted to favor a quasi-planar C_{2v} geometry at DFT level.[10] Recent extensive GM searches showed that complicated structural competitions exist in medium-sized B_n clusters, with C_2 B_{46} being the smallest core-shell boron cluster (B_4@B_{42}) reported to date and D_{2h} B_{48}, C_2 B_{54}, C_{2h} B_{60}, and C_1 B_{62} being the first bilayer boron clusters with a B_{38} bilayer hexagonal prism at the center surrounded by certain numbers of boron atoms on the waist.[9f,11] Encouragingly, bilayer D_{2h} $B_{48}^{-/0}$ clusters were very recently observed in a joint PES and first-principles theory investigation, providing the first experimental evidence for the viability of free-standing 2D bilayer borophenes similar to monolayer graphenes.[4] However, there has been no theoretical or experimental evidence reported to date on bilayer boron clusters beyond B_{62} where bilayer structures prevail over other geometries and the up-limit of bilayer boron nanoclusters at which the bilayer to core-shell structural transition occurs still remains unknown.

Based on extensive GM searches and first-principles theory calculations, we predict in this work the bilayer C_2 B_{64} (**I**), D_2 B_{66} (**II**), D_2 B_{68} (**III**), C_1 B_{70} (**IV**), and C_i B_{72} (**V**) as the GMs of the systems beyond B_{62} and the bilayer to core-shell structural transition at B_{74} where the most stable bilayer isomer obtained is found to be slightly less stable than the previously reported core-shell C_1 B_{74}[9d] in thermodynamics. The bilayer B_{64}, B_{66}, B_{68},

[a] Dr. L. Pei,[+] Dr. Q.-Q. Yan,[+] Prof. Dr. S.-D. Li
Institute of Molecular Science,
Shanxi University,
Taiyuan 030006, China
E-mail: lisidian@sxu.edu.cn
[b] Dr. L. Pei[+]
Department of Chemical Engineering and Safety,
Binzhou University,
Binzhou 256603, China
[+] L. Pei and Q.-Q. Yan contributed equally to this work.

Supporting information for this article is available on the WWW under https://doi.org/10.1002/ejic.202100328

B_{70}, and B_{72} all contain an elongated B_{46} bilayer hexagonal prism at the center surrounded by certain numbers of boron atoms on the waist, featuring four effective interlayer B–B σ bonds between eight inward-buckled boron atoms on the top and bottom layers. These highly stable bilayer nanoclusters follow the universal bonding pattern of σ+π double delocalization and are three dimensionally aromatic in nature.

Results and Discussions

Structures and Stabilities

The optimized bilayer C_2 B_{64} (**I**), D_2 B_{66} (**II**), D_2 B_{68} (**III**), C_1 B_{70} (**IV**), and C_i B_{72} (**V**) GMs are shown in Figure 1, with more alternative low-lying isomers depicted in Figure S1. The configurational energy spectra of B_{64}, B_{66}, B_{68}, B_{70}, and B_{72} are depicted in Figure 2 at PBE0/6-311+G(d) level. The calculated lowest-lying vibrational frequencies v_{min} at PBE0/6-31G(d) and HOMO-LUMO energy gaps ΔE_{gap}, cohesive energy per atom E_{coh}, and nucleus-independent chemical shifts (NICS)[12] at PBE0/6-311+G(d)[13] are comparatively tabulated in Table 1 for bilayer B_n clusters in the size range between $n=48$–72. The E_{coh}~n curves of B_n clusters (n=48–74) in different structural motifs are compared in Figure 3.

As shown in Figure S1a in the ESI†, eighteen out of the twenty lowset-lying isomers of B_{64} within 1.74 eV at PBE0/6-31G (d) all possess bilayer geometries. The axially chiral bilayer C_2 B_{64} (**I**) which can be obtained by adding a B_4 rhombus over the B_6 hexagonal window on the upper end of the previously reported

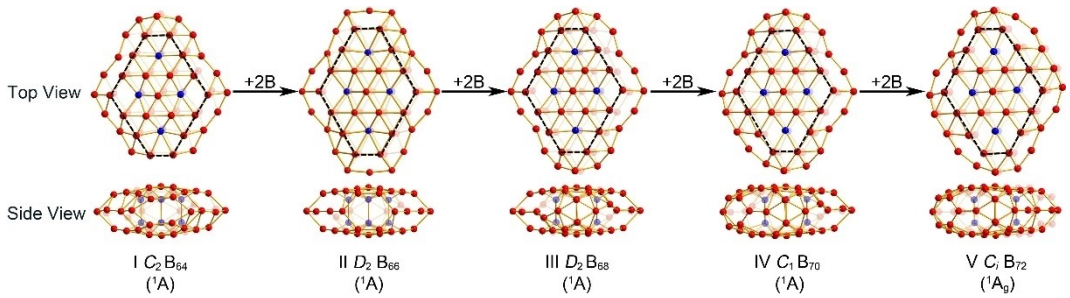

Figure 1. Top and side views of the optimized structures of C_2 B_{64} (**I**), D_2 B_{66} (**II**), D_2 B_{68} (**III**), C_1 B_{70} (**IV**), and C_i B_{72} (**V**) at PBE0/6-311+G(d) level. The elongated B_{46} bilayer hexagonal prisms at the center are highlighted in black circles and inward-buckled B atoms interconnected by four interlayer B–B bonds are colored in blue.

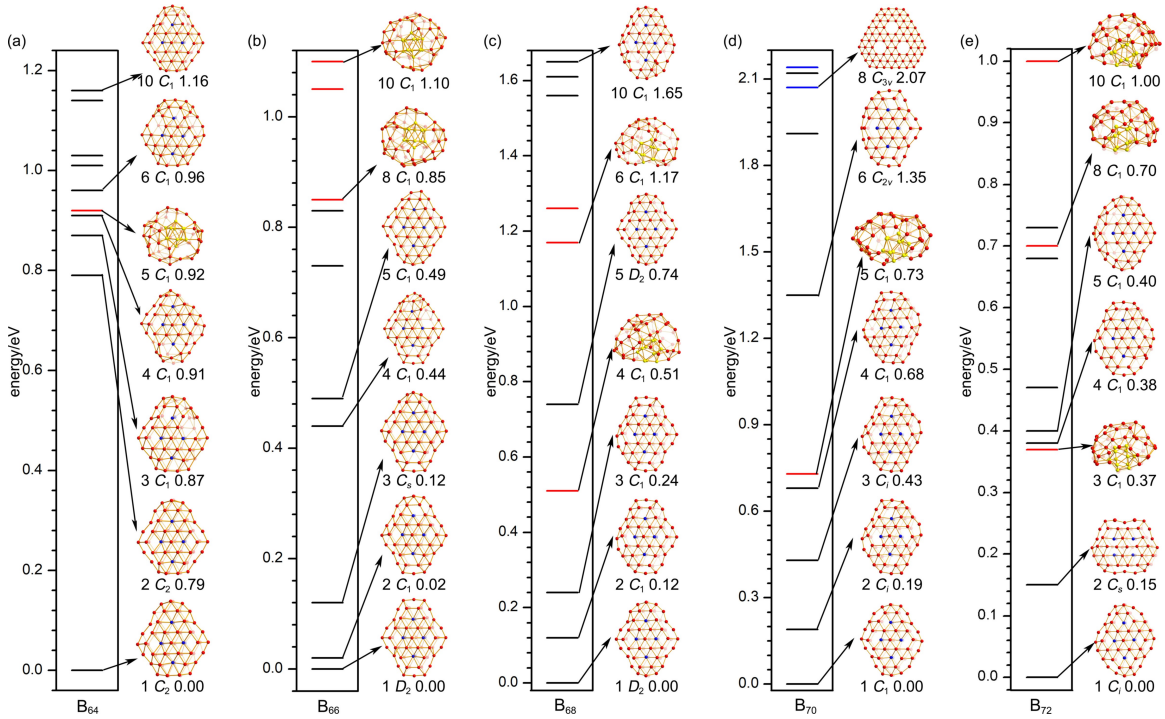

Figure 2. Configurational energy spectra of (**a**) B_{64}, (**b**) B_{66}, (**c**) B_{68}, (**d**) B_{70}, and (**e**) B_{72} at PBE0/6-311+G(d) level. Black, red and blue horizontal lines represent bilayer, core-shell and quasi-planar structures, respectively. Relative energies are given in eV.

Table 1. Comparison of the v_{min} (cm^{-1}), ΔE_{gap} (eV), E_{coh} (eV/atom) and NICS (ppm) values calculated for the bilayer B_n (n = 48–72) clusters reported to date.

B_n	v_{min} [cm^{-1}][a]	ΔE_{gap} [eV][b]	E_{coh} ([eV] atom)[b]	NICS [ppm][b]
D_{2h} B_{48}	75.11	1.49	−5.3433	−31.2
C_2 B_{54}	128.4	1.98	−5.3653	−33.2
C_{2h} B_{60}	105.5	1.14	−5.3646	−41.5
C_1 B_{62}	135.5	1.45	−5.3824	−31.4
C_2 B_{64}	110.7	1.54	−5.3858	−20.5
D_2 B_{66}	18.8	1.13	−5.3920	−33.3
D_2 B_{68}	137.5	1.47	−5.4025	−16.8
C_1 B_{70}	22.0	1.43	−5.4103	−12.3
C_i B_{72}	107.6	1.55	−5.4132	−5.7

[a] At PBE0/6-31G(d) level [b] At PBE0/6-311+G(d) level

C_{2h} B_{60}[11] contains an elongated B_{46} bilayer hexagonal prism at the center (highlighted in a black circle in Figure 1) surrounded by 18 B atoms on the waist. It features four effective interlayer B–B σ bonds between eight inward-buckled boron atoms (highlighted in blue) on the top and bottom layers. C_2 B_{64} (**I**) appears to be the well defined GM of B_{64} strongly favored in thermodynamics over other isomers (Figure 2a): it is 0.79 eV and 0.92 eV more stable than the second lowest-lying bilayer C_2 B_{64} and first lowest-lying core-shell C_1 B_{64} at PBE0/6-311+G(d), respectively (Figure S1a). The previously proposed cage-like D_{4d} B_{64}[14] proves to be much less stable than the C_2 GM (by 3.53 eV) at PBE0/6-31G(d) (Figure S1a).

The potential energy surface of B_{66} appears to be more congested (Figure 2b). Its seven lowest-lying isomers within 0.85 eV at PBE0/6-311+G(d) all possess bilayer configurations, with the axially chiral GM D_2 B_{66} (**II**) which can be obtained from the previously reported C_{2h} B_{60}[11] by adding two –B–B–B– chains over two B_6 hexagons on the upper and down ends being only 0.02 and 0.15 eV more stable than the second lowest-lying isomer bilayer C_1 B_{66} at PBE0/6-311+G(d) and TPSSh/6-311+G(d)[13a,15] (Figure S1b), respectively. These two close-lying bilayer isomers are practically iso-energetic in thermodynamics and may coexist in gas-phase experiments. The prototypical core-shell C_1 B_{66}, quasi-planar C_s B_{66}, cage-like D_2 B_{66}, and triple-ring tubular C_{2h} B_{66}[16] are found to be 0.84, 2.24, 3.43, and 4.15 eV less stable than B_{66} (**II**) at PBE0/6-31G(d), respectively (Figure S1b).

B_{68} is an object more concerned in this work. It has a complicated configurational competition between bilayer and core-shell isomers, with the core-shell isomers starting to appear as the fourth, sixth, and seventh lowest-lying isomers (Figure 2c and Figure S1c). An amorphous incomplete core-shell C_1 B_{68} with a partially encapsulated icosahedral B_{12} core was proposed by Zhao and co-workers in 2010 via unbiased GM searches.[9d] However, in conjunction with manual structural constructions based on known bilayer species, extensive GM searches performed in this work indicate that the high-symmetry axially chiral bilayer D_2 B_{68} (**III**) is 0.51 eV and 0.58 eV more stable than the previously reported core-shell C_1 B_{68}[9d] at PBE0/6-311+G(d) and TPSSh/6-311+G(d), respectively (Figure S1c), presenting a bilayer D_2 B_{68} as the GM of the system for future experiments to confirm. The second and third lowest-lying bilayer isomers also appear to be obviously more stable than core-shell C_1 B_{68} (Figure 3c). D_2 B_{68} (**III**) can be obtained either from the previously reported C_{2h} B_{60}[11] by adding two equivalent B_4 rhombuses over two B_6 hexagons on the upper and down ends or from D_2 B_{66} (**II**) by adding two penta-coordinate η^5-B atoms at the two ends. It possesses an elongated B_{46} bilayer hexagonal prism at the center sealed by 22 B atoms on the waist, featuring four effective interlayer B–B σ bonds formed between the top and bottom layers. The prototypical quasi-planar C_1 B_{68}, cage-like C_1 B_{68}, and hexa-ring tubular C_1 B_{68} are found to lie 2.98, 4.57, 4.57 eV higher than the bilayer D_2 GM at PBE0/6-31G(d), respectively (Figure S1c).

Adding two more boron atoms to D_2 B_{68} (**III**) to form a B_6 hexagonal window on one side of the waist generates the most

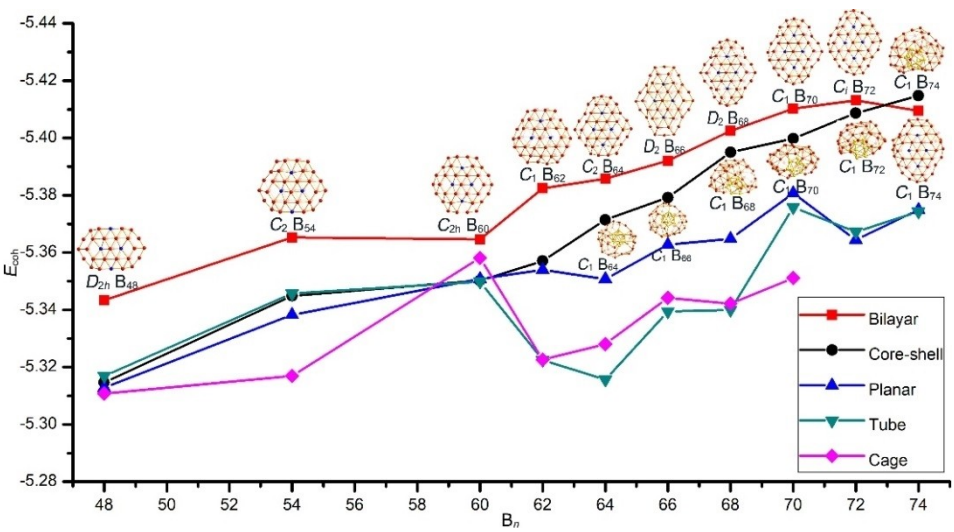

Figure 3. Binding energy per atom of the B_n clusters (n = 48–74) in different structural motifs: bilayer (squares), core-shell (circles), planar (triangles), tubular (inverted triangles), and cage-like (rhombuses).

stable bilayer C_1 B_{70} (**IV**) which lies 2.07 and 1.39 eV more stable than the previously predicted quasi-planar triplet C_{3v} B_{70} ($^3A_1$)[10] at PBE0/6-311+G(d) and TPSSh/6-311+G(d), respectively (Figure S1d). Five more bilayer isomers (the second, third, fourth, sixth, and seventh isomers) and one core-shell isomer (the fifth isomer) are found to be energetically more favorable than quasi-planar C_{3v} B_{70}. The tubular C_s B_{70} is found to lie 2.81 eV higher than B_{70} (**IV**) at PBE0/6-31G(d) (Figure S1d).

Addition of two more boron atoms to B_{70} generates more complicated structural competitions to the system. As shown in Figure 2e, bilayer C_i B_{72} (**V**) is the most stable isomer obtained for B_{72} in this work, with both the first (C_1) and second (C_1) lowset-lying core-shell isomers being 0.37 and 0.70 eV less stable than the bilayer GM at PBE0/6-311+G(d), respectively. B_{72} (**V**) can be obtained either from C_1 B_{70} (**IV**) by adding two more boron atoms to the system to form two symmetrically distributed B_6 hexagonal windows on two diagonal edges or from D_2 B_{68} (**III**) by adding four boron atoms to the system to form two equivalent B_6 hexagonal windows on two diagonal edges. Typical tubular and quasi-planar isomers appear to be at least 3.64 eV less stable than B_{72} (**V**) at PBE0/6-31G(d) (Figure S1e). It is noticed that B_{72} (**V**) possesses the highest cohesive energy per atom of $E_{coh}=-5.4132$ eV in the bilayer B_n series between n=48–72 (Table 1 and Figure 3) where, in overall, the bilayer species prevail in relative energies over planar, core-shell, and tubular structural motifs (Figure 3).

With two more boron atoms added in, a dramatic bilayer to core-shell structural transition occurs at B_{74} where the previously reported incomplete core-shell C_1 B_{74}[9d] appears to be slightly more stable than the most stable bilayer C_1 B_{74} obtained in this work by 0.40 eV and 0.27 eV at PBE0/6-311+G(d) and TPSSh/6-311+G(d) levels, respectively (Figure S1f). This observation defines C_i B_{72} (**V**) as the up-limit of the bilayer structural motif in medium-sized B_n clusters beyond which core-shell structures start to dominate in thermodynamics (Figure 3). The smallest core-shell B_n cluster is thus B_{74} at both PBE0 and TPSSh levels, instead of the previously predicted B_{68},[9d] with both B_{70} and B_{72} possessing bilayer GMs which are obviously more stable than their core-shell counterparts (Figure 2 and 3).

Bilayer B_{64} (**I**), B_{66} (**II**), B_{68} (**III**), B_{70} (**IV**), and B_{72} (**V**) with the large calculated HOMO-LUMO gaps of 1.54, 1.13, 1.47, 1.43, and 1.55 eV (Table 1) also appear to be dynamically stable, as demonstrated in Figure S2 for D_2 B_{66} (**II**) and D_2 B_{68} (**III**) which have the small average root-mean-square-deviations of RMSD= 0.13, 0.20 Å and maximum bond length deviations of MAXD= 0.66, 1.33 Å at 700 K, respectively (Figure S2). Similar situations exist in other bilayer species. These bilayer species which can be viewed as squashed cage-like structures all appear to be 3D aromatic in nature, as evidenced by their negative calculated NICS values NICS=−5.7~−33.3 ppm in the size range between n=64–72 (Table 1).

Bonding Analyses

To better interpret the high stabilities of these bilayer species, detailed AdNDP[17] bonding analyses were performed on the high-symmetry D_2 B_{66} (**II**) and D_2 B_{68} (**III**) in Figure 4. As shown in Figure 4a, B_{66} (**II**) possesses 4 interlayer 2c–2e B–B σ-bonds between eight inward-buckled B atoms on the top and bottom layers with the occupation numbers of ON=1.80–1.87 |e|, 28 2c–2e B–B σ-bonds on the waist with ON=1.73–1.83 |e|, 40 3c–2e σ bonds on the top and bottom layers with ON=1.78–1.93 |e|, 2 5c–2e σ bonds at two corners on the left and right with ON=1.73 |e|, 6 9c–2e σ bonds on the upper and down ends with ON=1.85–1.95 |e|, and 1 14c–2e σ bond at the center between the top and bottom layers with ON=1.77 |e|. The remaining 18 delocalized π bonds are divided into four categories over the σ-skeleton, including 2 5c–2e π bonds at two corners on the left and right with ON=1.88 |e|, 8 6c–2e π bonds on the top and bottom layers around the central region with ON=1.82–1.83 |e|, 2 7c–2e π bonds over two B_7 hexagonal pyramids at the center on the top and bottom layers with ON=1.79 |e|, and 6 17c–2e π bonds at the upper and down ends with ON=1.80–1.92 |e|. Such a bonding pattern in an overall symmetry of D_2 follows the universal bonding pattern of σ+π double delocalization observed in bilayer B_{48}, B_{54}, and B_{62}[11] and the B_n^q borospherene family (n=36–42, q=n-40).[3,5]

D_2 B_{68} (**III**) exhibits a similar bonding pattern (Figure 4b) with D_2 B_{66} (**II**). It has 84 σ-bonds in total, including 4 interlayer 2c–2e σ bonds between eight inward-buckled B atoms in the top and bottom layers, 28 2c–2e σ bonds on the waist, 48 3c–2e σ bonds on the top and bottom layers, 2 5c–2e σ bonds at two corners on the left and right, and 2 7c–2e σ bonds on the two B_7 hexagonal pyramids on the top and bottom layers at the center. The corresponding π system includes 2 5c–2e π bonds at two corners on the left and right, 8 6c–2e π bonds around the central region on the top and bottom layers, 2 7c–2e π bonds at the centers of the top and bottom layers, and 6 18c–2e π bonds around the upper and down ends of the bilayer structure. The universal σ+π double delocalization bonding pattern renders 3D aromaticity to the bilayer B_n cluster series with n=48, 54, 60, 64, 66, 68, 70, and 72, as evidenced by their calculated negative NICS values of NICS=−41.5~−5.7 ppm at their geometrical centers (Table 1). These bilayer species possess the large calculated HOMO-LUMO gaps between ΔE_{gap}=1.13~1.98 eV, showing their high chemical stabilities in gas phases, with C_2 B_{54} and C_i B_{72} possessing the largest ΔE_{gap}= 1.98 eV and 1.55 eV, respectively (Table 1).

Spectral Simulations

To facilitate future spectral characterizations of these bilayer species, we simulate the infrared (IR), Raman, and UV-vis spectra of D_2 B_{66} (**II**) and D_2 B_{68} (**III**) in Figure 5. B_{66} (**II**) exhibits five strong IR peaks at 231 cm^{-1} (b_2), 273 cm^{-1} (b_2), 958 cm^{-1} (b_3), 1135 cm^{-1} (b_2), and 1433 cm^{-1} (b_3), while D_2 B_{68} (**III**) possesses three intensive IR active modes at 824 cm^{-1} (b_3), 936 cm^{-1} (b_3), and 1435 cm^{-1} (b_3), respectively. B_{66} (**II**) has two major Raman active vibrational modes at 811 cm^{-1} (a) and 1421 cm^{-1} (a) and D_2 B_{68} (**III**) exhibits two strong Raman bands at 839 cm^{-1} (a) and 851 cm^{-1} (a), respectively. The weak vibrational modes at 275 cm^{-1} (a) in D_2 B_{66} (**II**) and 255 and 320 cm^{-1} in D_2 B_{68} (**III**)

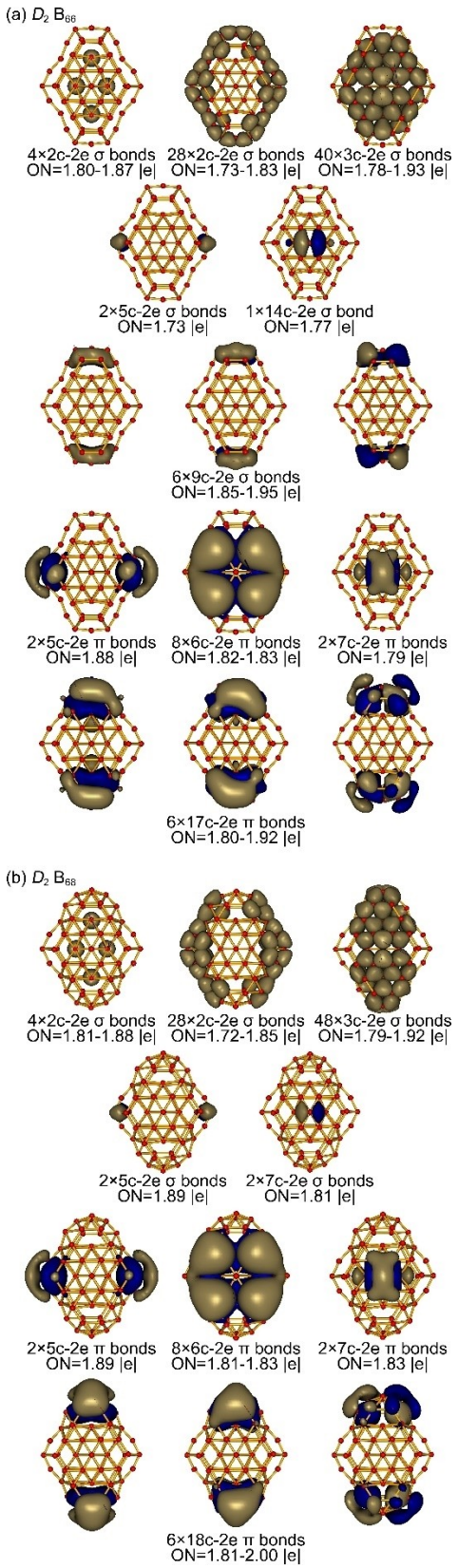

Figure 4. AdNDP bonding patterns of (a) D_2 B_{66} (**II**) and (b) D_2 B_{68} (**III**).

represent typical "radial breathing modes" (RBMs)[18] of the two bilayer structures at PBE0/6-31G(d) which can be used to characterize hollow boron nanostructures.

The strong UV absorption peak of D_2 B_{66} (**II**) occurs at 324 nm ($^1B_3$) which mainly originates from the S0→S327 electronic excitation with major contributions from HOMO-16→LUMO+2 (25%) and HOMO–4→LUMO+11 (19%) transitions (Table S1). The other strong absorptions at 375 ($^1B_3$), 388 ($^1B_3$) and 444 ($^1B_3$) nm also correspond to the excitations from the occupied inner shells to unoccupied frontier orbitals. The strongest UV absorption peak of D_2 B_{68} (**III**) at 315 nm ($^1B_3$) corresponds to the electronic transition of S0→S365 with major contributions from HOMO-9→LUMO+8 (22%) and HOMO–11→LUMO+5 (25%) (Table S1).

Summary

Based on extensive GM searches and manual structural constructions, we have expanded in this work the bilayer boron cluster series from the previously reported D_{2h} B_{48}, C_2 B_{54}, C_{2h} B_{60}, and C_1 B_{62}[11] to C_2 B_{64} (**I**), D_2 B_{66} (**II**), D_2 B_{68} (**III**), C_1 B_{70} (**IV**), and C_i B_{72} (**V**) where bilayer configurations dominate and predicted the bilayer to core-shell structural transition at B_{74} where a core-shell isomer starts to prevail in thermodynamics. The bilayer **I**–**V** all contain an elongated B_{46} hexagonal prism at the center which features four effective interlayer 2c–2e B–B σ bonds formed between the top and bottom layers. Such 3D aromatic bilayer boron nanoclusters follow the universal bonding pattern of σ+π double delocalization and may be used as building blocks to form stable 2D free-standing bilayer borophenes partially passivated via the formation of effective interlayer B–B σ bonds and weak interlayer π-π stacking.

Theoretical procedures

The GMs of B_{64}, B_{66}, B_{68}, B_{70}, and B_{72} were searched using the TGMin program[19] at the PBE level,[20] in conjunction with manual structural constructions based on the previously predicted bilayer B_{48}, B_{54}, B_{60}, and B_{62}.[9f,11] Low-lying isomers were firstly reoptimized at the PBE0/6-31G(d), with vibrational frequencies checked (Table 1) and zero-point corrections encluded. To achieve more reliable relative energies, the five lowest-lying isomers of B_{64}, B_{66}, B_{68}, B_{70}, and B_{72} were further reoptimized at the PBE0/6-311+G(d)[13] and TPSSh/6-311+G(d)[13a,15] levels, respectively. Detailed chemical bonding analyses were carried out on the high-symmetry D_2 B_{66} (**II**) and D_2 B_{68} (**III**) utilizing the adaptive natural density partitioning (AdNDP)[17] approach at PBE0/6-31G, with the bonding patterns visualized utilizing the Molekel software.[21] The IR and Raman spectra of D_2 B_{66} (**II**) and D_2 B_{68} (**III**) were simulated at PBE0/6-31G(d) level and their UV-vis absorption spectra calculated using the time-dependent density functional method (TD-DFT-PBE0).[22] All the calculations in this work were done using the Gaussian16 package.[23] Extensive Born-Oppenheimer molecular dynamics (BOMD) simulations were performed on the D_2 B_{66} (**II**) and D_2 B_{68}

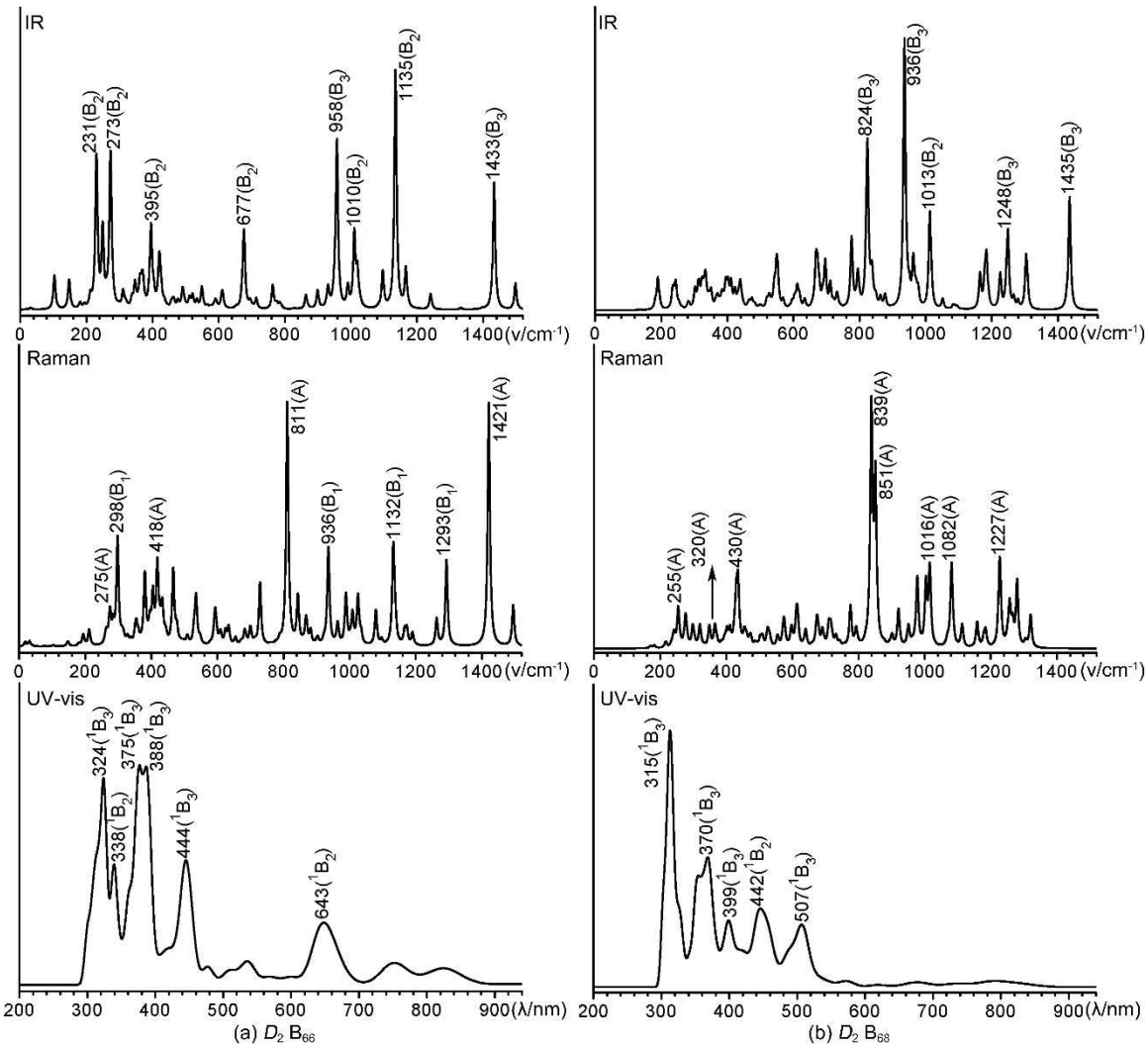

Figure 5. Simulated IR, Raman, and UV-vis of (a) D_2 B_{66} (**II**) and (b) D_2 B_{68} (**III**) at PBE0/6-31G(d) level.

(**III**) at 700 K for 30 ps, using the software suite CP2K[24] with the GTH-PBE pseudopotential and DZVP-MOLOPT-SR-GTH basis set.

Acknowledgements

This work was supported by the National Natural Science Foundation of China (21720102006 and 21973057 to S.-D. Li).

Conflict of Interest

The authors declare no conflict of interest.

Keywords: Boron Clusters · Density Functional Theory · Structures, Bonding · Three-Dimensional Aromaticity · Bilayer Borophenes

[1] a) A. P. Sergeeva, I. A. Popov, Z. A. Piazza, W. L. Li, C. Romanescu, L. S. Wang, A. I. Boldyrev, *Acc. Chem. Res.* **2014**, *47*, 1349–1358; b) T. N. Gribanova, R. M. Minyaev, V. I. Minkin, A. I. Boldyrev, *Struct. Chem.* **2020**, *31*, 2105–2128.

[2] a) J. K. Olson, A. I. Boldyrev, *J. Phys. Chem. A* **2013**, *117*, 1614–1620; b) A. N. Alexandrova, A. I. Boldyrev, H. J. Zhai, L. S. Wang, *Coord. Chem. Rev.* **2006**, 250, 2811–2866; c) L. S. Wang, *Int. Rev. Phys. Chem.* **2016**, *35*, 69–142; d) T. Jian, X. N. Chen, S. D. Li, A. I. Boldyrev, J. Li, L. S. Wang, *Chem. Soc. Rev.* **2019**, *48*, 3550–3591; e) H. Bai, T. T. Chen, Q. Chen, X. Y. Zhao, Y. Y. Zhang, W. J. Chen, Wa. L. Li, L. F. Cheung, B. Bai, J. Cavanagh, W. Huang, S. D. Li, J. Li, L. S. Wang, *Nanoscale* **2019**, *11*, 23286–23295.

[3] a) Q. Chen, W. L. Li, Y. F. Zhao, S. Y. Zhang, H. S. Hu, H. Bai, H. R. Li, W. J. Tian, H. G. Lu, H. J. Zhai, S. D. Li, J. Li, L. S. Wang, *ACS Nano.* **2015**, *9*, 754–760; b) H. J. Zhai, Y. F. Zhao, W. L. Li, Q. Chen, H. Bai, H. S. Hu, Z. A. Piazza, W. J. Tian, H. G. Lu, Y. B. Wu, Y. W. Mu, G. F. Wei, Z. P. Liu, J. Li, S. D. Li, L. S. Wang, *Nat. Chem.* **2014**, *6*, 727–731.

[4] W. J. Chen, Y. Y. Ma, T. T. Chen, M. Z. Ao, D. F. Yuan, Q. Chen, X. X. Tian, Y. W. Mu, S. D. Li, L. S. Wang, *Nanoscale* **2021**, *13*, 3868–3876.

[5] a) Q. Chen, S. Y. Zhang, H. Bai, W. J. Tian, T. Gao, H. R. Li, C. Q. Miao, Y. W. Mu, H. G. Lu, H. J. Zhai, S. D. Li, *Angew. Chem. Int. Ed.* **2015**, *54*, 8160–8164; *Angew. Chem.* **2015**, *127*, 8278–8282; b) Q. Chen, H. R. Li, W. J. Tian, H. G. Lu, H. J. Zhai, S. D. Li, *Phys. Chem. Chem. Phys.* **2016**, *18*, 14186–14190; c) Q. Chen, H. R. Li, C. Q. Miao, Y. J. Wang, H. G. Lu, T. Gao, Y. W. Mu, G. M. Ren, H. J. Zhai, S. D. Li, *Phys. Chem. Chem. Phys.* **2016**, *18*, 11610–11615; d) W. J. Tian, Q. Chen, H. R. Li, M. Yan, Y. W. Mu, H. G. Lu, H. J. Zhai, S. D. Li, *Phys. Chem. Chem. Phys.* **2016**, *18*, 9922–9926.

[6] a) Y. J. Wang, Y. F. Zhao, W. L. Li, T. Jian, Q. Chen, X. R. You, T. Ou, X. Y. Zhao, H. J. Zhai, S. D. Li, J. Li, L. S. Wang, *J. Chem. Phys.* **2016**, *144*, 064307; b) H. R. Li, T. Jian, W. L. Li, C. Q. Miao, Y. J. Wang, Q. Chen, X. M. Luo, K. Wang, H. J. Zhai, S. D. Li, L. S. Wang, *Phys. Chem. Chem. Phys.* **2016**, *18*, 29147–29155.
[7] a) L. Pei, H. R. Li, M. Yan, Q. Chen, Y. W. Mu, H. G. Lu, Y. B. Wu, S. D. Li, *Phys. Chem. Chem. Phys.* **2018**, *20*, 15330–15334; b) L. Pei, M. Yan, X. Y. Zhao, Y. W. Mu, H. G. Lu, Y. B. Wu, S. D. Li, *RSC Adv.* **2020**, *10*, 10129–10133; c) H. Liu, Q. Chen, H. R. Li, X. Y. Zhao, X. X. Tian, Y. W. Mu, H. G. Lu, S. D. Li, *Phys. Chem. Chem. Phys.* **2018**, *20*,15344–15349; d) H. Liu, Y. W. Mu, S. D. Li, *J. Cluster Sci.* DOI:10.1007/s10876-020-01943-z.
[8] E. Oger, N. R. Crawford, R. Kelting, P. Weis, M. M. Kappes, R. Ahlrichs, *Angew. Chem. Int. Ed.* **2007**, *46*, 8503–8506; *Angew. Chem.* **2007**, *119*, 8656–8659.
[9] a) M. Zhang, H. G. Lu, S. D. Li, *Nano Res.* DOI:10.1007/s12274-021-3411-x; b) D. L. Prasad, E. D. Jemmis, *Phys. Rev. Lett.* **2008**, *100*, 165504; c) H. Li, N. Shao, B. Shang, L. F. Yuan, J. Yang, X. C. Zeng, *Chem. Commun.* **2010**, *46*, 3878–3880; d) J. J. Zhao, L. Wang, F. Y. Li, Z. F. Chen, *J. Phys. Chem. A* **2010**, *114*, 9969–9972; e) F. Y. Li, P. Jin, D. E. Jiang, L. Wang, S. B. B. Zhang, J. J. Zhao, Z. F. Chen, *J. Chem. Phys.* **2012**, *136*, 074302; f) L. W. Sai, X. Wu, N. Gao, J. J. Zhao, R. B. King, *Nanoscale* **2017**, *9*, 13905–13909.
[10] A. B. Rahane, V. Kumar, *Nanoscale* **2015**, *7*, 4055–4062.
[11] L. Pei, Y. Y. Ma, M. Yan, M. Zhang, R. N. Yuan, Q. Chen, W. Y. Zan, Y. W. Mu, S. D. Li, *Eur. J. Inorg. Chem.* **2020**, 3296–3301.
[12] a) P. V. R. Schleyer, C. Maerker, A. Dransfeld, H. J. Jiao, N. J. R. V. E. Hommes, *J. Am. Chem. Soc.* **1996**, *118*, 6317–6318; b) Z. F. Chen, C. S. Wannere, C. Corminboeuf, R. Puchta, P. V. R. Schleyer, *Chem. Rev.* **2005**, *105*, 3842–3888.
[13] a) R. Krishnan, J. S. Binkley, R. Seeger, J. A. Pople, *J. Chem. Phys.* **1980**, *72*, 650–654; b) C. Adamo, V. Barone, *J. Chem. Phys.* **1999**, *110*, 6158–6170.
[14] Q. B. Yan, X. L. Sheng, Q. R. Zheng, L. Z. Zhang, G. Su, *Phys. Rev. B* **2008**, *78*, 201401.
[15] V. N. Staroverov, G. E. Scuseria, J. Tao, J. P. Perdew, *J. Chem. Phys.* **2003**, *119*, 12129–12137.
[16] F. Y. Tian, Y. X. Wang, *J. Chem. Phys.* **2008**, *129*, 024903.
[17] a) N. V. Tkachenko, A. I. Boldyrev, *Phys. Chem. Chem. Phys.* **2019**, *21*, 9590–9596; b) D. Y. Zubarev, A. I. Boldyrev, *Phys. Chem. Chem. Phys.* **2008**, *10*, 5207–5217; c) D. Y. Zubarev, A. I. Boldyrev, *J. Org. Chem.* **2008**, *73*, 9251–9258.
[18] D. Ciuparu, R. F. Klie, Y. M. Zhu, L. Pfefferle, *J. Phys. Chem. B* **2004**, *108*, 3967–3969.
[19] a) Y. F. Zhao, X. Chen, J. Li, *Nano Res.* **2017**, *10*, 3407–3420; b) X. Chen, Y. F. Zhao, L. S. Wang, J. Li, *Comput. Theor. Chem.* **2017**, *1107*, 57–65; c) X. Chen, Y. F. Zhao, Y. Y. Zhang, J. Li, *J. Comput. Chem.* **2019**, *40*, 1105–1112.
[20] J. P. Perdew, K. Burke, M. Ernzerhof, *Phys. Rev. Lett.* **1996**, *77*, 3865–3868.
[21] U. Varetto, Molekel 5.4.0.8, Swiss National Supercomputing Center, Manno, Switzerland, **2009**.
[22] a) R. Bauernschmitt, R. Ahlrichs, *Chem. Phys. Lett.* **1996**, *256*, 454–464; b) M. E. Casida, C. Jamorski, K. C. Casida, D. R. Salahub, *J. Chem. Phys.* **1998**, *108*, 4439–4449.
[23] M. J. Frisch, G. W. Trucks, H. B. Schlegel, G. E. Scuseria, M. A. Robb, J. R. Cheeseman, G. Scalmani, V. Barone, G. A. Petersson, H. Nakatsuji, X. Li, M. Caricato, A. V. Marenich, J. Bloino, B. G. Janesko, R. Gomperts, B. Mennucci, H. P. Hratchian, J. V. Ortiz, A. F. Izmaylov, J. L. Sonnenberg, D. Williams-Young, F. Ding, F. Lipparini, F. Egidi, J. Goings, B. Peng, A. Petrone, T. Henderson, D. Ranasinghe, V. G. Zakrzewski, J. Gao, N. Rega, G. Zheng, W. Liang, M. Hada, M. Ehara, K. Toyota, R. Fukuda, J. Hasegawa, M. Ishida, T. Nakajima, Y. Honda, O. Kitao, H. Nakai, T. Vreven, K. Throssell, J. A. Montgomery, Jr., J. E. Peralta, F. Ogliaro, M. J. Bearpark, J. J. Heyd, E. N. Brothers, K. N. Kudin, V. N. Staroverov, T. A. Keith, R. Kobayashi, J. Normand, K. Raghavachari, A. P. Rendell, J. C. Burant, S. S. Iyengar, J. Tomasi, M. Cossi, J. M. Millam, M. Klene, C. Adamo, R. Cammi, J. W. Ochterski, R. L. Martin, K. Morokuma, O. Farkas, J. B. Foresman, D. J. Fox, *Gaussian 16*, Revision C.01, Gaussian, Inc., Wallingford CT, **2016**.
[24] J. V. Vondele, M. Krack, F. Mohamed, M. Parrinello, T. S. Chassaing, J. Hutter, *Comput. Phys. Commun.* **2005**, *167*, 103–128.

Manuscript received: April 23, 2021
Revised manuscript received: May 31, 2021
Accepted manuscript online: June 2, 2021